ChemSusChem

Research Article
doi.org/10.1002/cssc.202201901

Chemistry Europe
European Chemical Societies Publishing

www.chemsuschem.org

Novel Sb–SnO_2 Electrode with Ti^{3+} Self-Doped Urchin-Like Rutile TiO_2 Nanoclusters as the Interlayer for the Effective Degradation of Dye Pollutants

Shuaishuai Man[+],[a, b] Zehao Yin[+],[a] Shanbin Zhou,[a] Emmanuel Pameté,[b] Lei Xu,[a] Hebin Bao,[a] Wenjing Yang,[a] Zhihong Mo,[a] Volker Presser,*[b, c, d] and Xueming Li*[a]

Stable and efficient SnO_2 electrodes are very promising for effectively degrading refractory organic pollutants in wastewater treatment. In this regard, we firstly prepared Ti^{3+} self-doped urchin-like rutile TiO_2 nanoclusters (TiO_{2-x}NCs) on a Ti mesh substrate by hydrothermal and electroreduction to serve as an interlayer for the deposition of Sb–SnO_2. The TiO_{2-x}NCs/Sb–SnO_2 anode exhibited a high oxygen evolution potential (2.63 V vs. SCE) and strong •OH generation ability for the enhanced amount of absorbed oxygen species. Thus, the degradation results demonstrated its good rhodamine B (RhB), methylene blue (MB), alizarin yellow R (AYR), and methyl orange (MO) removal performance, with the rate constant increased 5.0, 1.9, 1.9, and 4.7 times, respectively, compared to the control Sb–SnO_2 electrode. RhB and AYR degradation mechanisms are also proposed based on the results of high-performance liquid chromatography coupled with mass spectrometry and quenching experiments. More importantly, this unique rutile interlayer prolonged the anode lifetime sixfold, given its good lattice match with SnO_2 and the three-dimensional concave–convex structure. Consequently, this work paves a new way for designing the crystal form and structure of the interlayers to obtain efficient and stable SnO_2 electrodes for addressing dye wastewater problems.

Introduction

With rapid industrial expansion and accelerated urbanization, water pollution is a severe concern to humankind and the environment.[1] Dye wastewater, in particular, has remained a challenge due to its nonbiodegradability, high toxicity to life forms, strong chemical stability for the aromatic structure, and tremendous dye output (about two million tons worldwide per year).[2] The high color intensity also detriment the aquatic diversity by blocking sunlight from passing through the water. To date, various strategies, including adsorption,[3] photodegradation,[4] and biodegradation,[5] are explored and used for dye wastewater remediation, albeit further improvements are needed for its incomplete mineralization or low efficiency.[6]

Electrochemical oxidation is promising for removing persistent dye contaminants because it is chemical-free, easy to operate, and has a high oxidation capacity.[7] The anode materials directly determine the degradation performance for controlling the generation capacity of strong oxidizing hydroxyl radicals (•OH).[8] Inert anodes, such as boron-doped diamond (BDD),[9] PbO_2,[10] and Sb–SnO_2,[11] often exhibit excellent dye contaminants decomposition performance given to their high oxygen evolution overpotential (OEP). In our previous work,[12] we achieved 94.6% chemical oxygen demand mineralization efficiency and almost 100% decolorization efficiency after 3.0 h electrolysis by the Ti/Sb–SnO_2NFs/PbO_2 anode for the degradation of methylene blue (MB). However, the possible leakage of harmful Pb^{2+} ions may pose an environmental issue. BDD's fragile and costly features are also detrimental to its large-scale application.[13] Consequently, Sb–SnO_2 is a very promising electrode material for destructing refractory pollutants owing to its low cost, environmental compatibility, high OEP, and economical energy consumption.[14] Nevertheless, it also comes up against some limitations, especially the unsatisfied stability and insufficient catalytic activity.[15]

Introducing TiO_2 nanotubes (TiO_2NTs) middle layer is a widely used strategy to overcome the bottlenecks mentioned

[a] Dr. S. Man,[+] Z. Yin,[+] S. Zhou, Dr. L. Xu, Dr. H. Bao, Prof. W. Yang, Prof. Z. Mo, Prof. X. Li
College of Chemistry and Chemical Engineering
Chongqing University
Chongqing 401331 (P. R. China)
E-mail: xuemingli@cqu.edu.cn
[b] Dr. S. Man,[+] Dr. E. Pameté, Prof. V. Presser
INM – Leibniz Institute for New Materials
66123, Saarbrücken (Germany)
E-mail: volker.presser@leibniz-inm.de
[c] Prof. V. Presser
Department of Materials Science and Engineering
Saarland University
66123, Saarbrücken (Germany)
[d] Prof. V. Presser
Saarene – Saarland Center for Energy Materials and Sustainability
Saarland University
Campus D4 2, 66123 Saarbrücken (Germany)
[+] These authors contributed equally to this work.

Supporting information for this article is available on the WWW under https://doi.org/10.1002/cssc.202201901

This publication is part of a Special Collection highlighting "The Latest Research from our Board Members". Please visit the Special Collection at chemsuschem.org/collections.

above, owing to the increased binding force between the Ti substrate and the Sb–SnO_2 coating layer and the enhanced OEP value.[16] For example, Pupo et al. fabricated a TiO_2NTs interlayer by employing a two-step electrochemical anodization method. The Ti/TiO_2NT/SnO_2-SbBi electrode yielded an almost 4-fold longer lifetime for forming fewer cracks and increased OEP value by +0.2 V.[17] Huang et al. also demonstrated the promoted •OH generation ability (increased about 2.2 times) of the Sb–SnO_2 electrode after adding the TiO_2NTs interlayer by anodization technology.[18] While promising, these works also showed the need for further improvements: The anodization process often proceeded at high voltage (25 V,[19] 42 V,[20] 60 V[21]) in corrosive or toxic fluorine-containing electrolytes (HF,[22] NH_4F[23]), which is not only energy intensive but also brought new environment concerns.[24] The anatase TiO_2NTs interlayer has a different crystal structure from rutile SnO_2, which is detrimental to the epitaxial growth of the SnO_2 coating layer.[25] As a semiconductor, the poor conductivity of TiO_2NTs also limits its large-scale application.[26]

In this regard, from the perspective of interlayer crystal form and structure, we first designed urchin-like rutile TiO_2 nanoclusters (TiO_2NCs) as the interlayer to prepare a novel Sb–SnO_2 electrode by hydrothermal and electrochemical deposition technologies. Compared to the anodization process to fabricate TiO_2 interlayer, the hydrothermal technology is free of toxic fluoride, allows control of the TiO_2 morphology, and is suitable for different substrates.[27] The obtained three-dimensional (3D) TiO_2 nanoclusters not only furnish more active sites for Sb–SnO_2 loading due to their conical structure but are also well-adapted to decrease the SnO_2 particle size.[28] We successfully adopted self-doping to introduce Ti^{3+} into the TiO_2 lattice to narrow its band gap further and create more oxygen vacancies.[29] These changes improve the TiO_2NCs electroconductivity to promote the current evenly distribution during electrodeposition.[30] Consequently, the novel Sb–SnO_2 electrode with Ti^{3+} modified TiO_2NCs as the interlayer (TiO_{2-x}NCs/Sb–SnO_2) achieved a satisfactory degradation efficiency for i) cationic dyes, rhodamine B (RhB) and methylene blue (MB), and ii) anionic dyes, alizarin yellow R (AYR) and methyl orange (MO). The 3D rutile TiO_{2-x}NCs interlayer also improves its binding force with the rutile Sb–SnO_2 coating layer given to the good lattice match and the concave-convex porous matrix structure (similar to the mortise-tenon structure found, for example, in traditional Chinese architecture). Therefore, this work provides a new avenue for the rational design of efficient and stable Sb–SnO_2 electrodes from interlayer crystal form and micro-structure for dye wastewater treatment. Hence, the proposed novel TiO_{2-x}NCs matrix can also be applied to prepare other electrodes, like PbO_2, MnO_2, or RuO_2.

Results and Discussion

Electrode characterization

As shown in Figure 1, the preparation procedures of the TiO_{2-x}NCs/Sb–SnO_2 electrode mainly involved three steps: fabricating

Figure 1. Preparation procedures of the TiO_{2-x}NCs/Sb–SnO_2 electrode.

the TiO_2NCs, TiO_{2-x}NCs, and Sb–SnO_2 layers by the hydrothermal method, electrochemical reduction, and electrodeposition technology, respectively. In the Supporting Information, Figure S1A and B, we demonstrate the successful preparation of urchin-like TiO_2 nanoclusters. The latter were self-assembled by TiO_2 nanocones, which contribute to providing a great number of nucleation sites for the Sb–Sn alloy. No noticeable morphology changes could be seen after the electrochemical reduction procedure, with the diameter of these nanoclusters being about 4–5 μm (Figure 2A–C), but the color is changed from white to blue-black (Supporting Information, Figure S1C in the Supporting Information). The nanoclusters are uniformly spread across the Ti mesh substrate, and cracks are not generated on the TiO_{2-x}NCs layer surface due to the sufficient space between nanocones to reduce internal stress. The homogenous coverage of the TiO_{2-x}NCs layer could provide a barrier to the penetration of the electrolyte and nascent oxygen into the titanium substrate, which is propitious to improve the anode stability. Only Ti and O elements are detected from the EDX spectrum (Supporting Information, Figure S2A) with a homogeneous distribution (Figure 2D, E). The atomic percentage of O decreased from 67.3% (with the atomic ratio of O to Ti was 2.1) to 60.3% (with the atomic ratio of O to Ti was 1.5) after the reduction process (Supporting Information, Figure S2B), suggesting the formation of oxygen defects and Ti^{3+} of the TiO_{2-x}NCs electrode.[29] The EPR spectra of the interlayers are shown in Supporting Information, Figure S2C. Compared to TiO_2NCs, TiO_{2-x}NCs presented a stronger EPR signal centered on $g = 2.004$ due to the formation of O_V and Ti^{3+}.[31] This observation is also in good agreement with the XPS results. As shown in Supporting Information, Figure S3A, the O 1s spectra of the TiO_2NCs electrode only include the lattice oxygen (O_L, 530.08 eV) and the adsorbed oxygen (O_{ad}, 531.69 eV). For TiO_{2-x}NCs (Supporting Information, Figure S3B), the oxygen vacancies (O_V) can be detected at 531.43 eV.[32] In Figure 2F, two peaks of Ti $2p_{3/2}$ (458.89 eV) and Ti $2p_{1/2}$ (464.63 eV) are presented on the Ti 2p detailed spectrum of the TiO_2NCs electrode. For comparison, for TiO_{2-x}NCs, these peaks are located at 459.04 eV and 464.83 eV for Ti $2p_{3/2}$ and Ti $2p_{1/2}$, respectively. The positive shift of the binding energy was also reported in previous works,[33] which may be due to the local electronic structure modifications effects or the over-reduction.[34] Four peaks are fitted for the Ti 2p spectrum of the

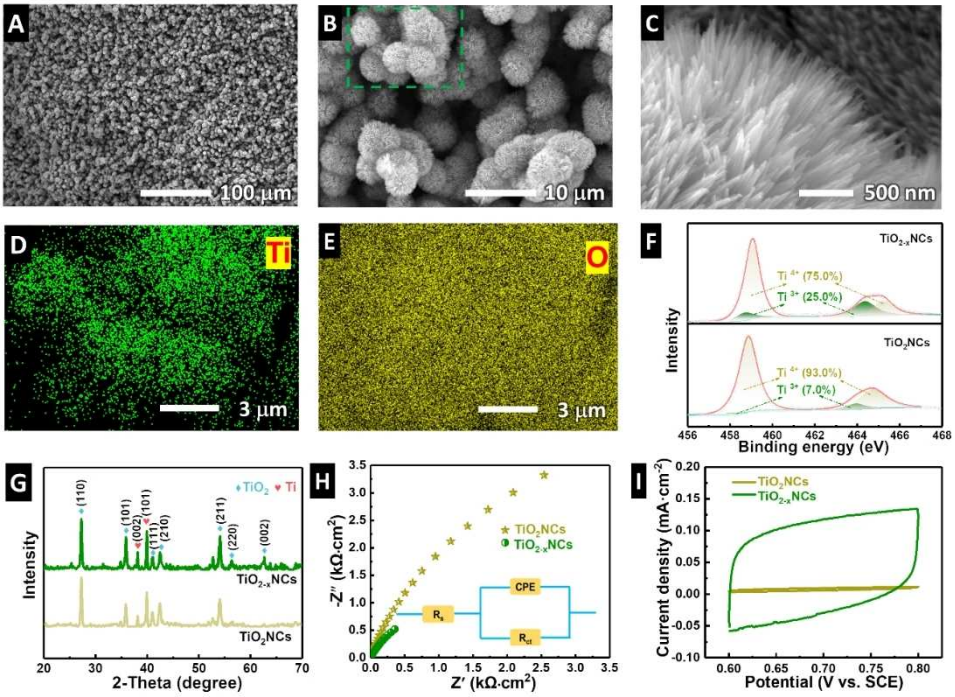

Figure 2. Scanning electron micrographs es of the prepared TiO_{2-x}NCs interlayer (A–C) and the corresponding elemental mapping images (D and E). Detailed Ti 2p spectrum (F), X-ray diffractograms (G), Nyquist plots (H), and cyclic voltammograms (I) of the prepared TiO_2NCs and TiO_{2-x}NCs interlayers.

TiO_{2-x}NCs electrode. Among them, the two peaks with the binding energy of 458.70 eV and 464.35 eV can be assigned to Ti^{3+}, and the other two peaks at 459.08 eV and 465.20 eV are ascribed to Ti^{4+}. Notably, the TiO_{2-x}NCs electrode possesses a much increased Ti^{3+} content (from 7.0% to 25.0%) than the given one. These results demonstrated the generation of oxygen defects and Ti^{3+} after the electrochemical reduction procedure, which forms trapped electrons and narrows the inherent bandgap of TiO_{2-x}NCs to improve its electrochemical conductivity.[35]

The corresponding X-ray diffractograms of the TiO_{2-x}NCs electrode (Figure 2G) demonstrate the successful formation of rutile TiO_2 (JCPDS No. 21-1276), which could form solid solutions with rutile SnO_2.[36] Compared with TiO_2NCs, the increased intensity of the (101) plane of TiO_{2-x}NCs indicate its preferred orientation in this direction. The cell volume of the TiO_{2-x}NCs is enlarged after the electrochemical reduction procedure (Table S1) due to the formation of Ti^{3+} in the TiO_2 lattice for its larger ionic radii (0.81 Å) than Ti^{4+} (0.74 Å).[37] The Raman data (Supporting Information, Figure S3C) confirm the phase of TiO_{2-x}NCs is rutile for the presence of three vibration modes B_{1g} (144 cm^{-1}), E_g (446 cm^{-1}), and A_{1g} (611 cm^{-1}). In Supporting Information, Figure S3D, we see a blue shift of the B_{1g} peak (from 143 cm^{-1} to 144 cm^{-1}) appears on TiO_{2-x}NCs with a prominent peak broadening owing to the effects of lattice distortion caused by the replacement of Ti^{3+} to Ti^{4+}, or oxygen defects as previously reported.[23,33a,38]

We carried out EIS measurements in 0.5 M H_2SO_4 to investigate the interfacial properties of the prepared interlayers. The obtained Nyquist plots are fitted by adopting the (R(CR)) equivalent circuit model (Figure 2H). R_s and R_{ct} represent the solution resistance and charge transfer resistance, respectively. CPE is the constant phase element. As summarized in Supporting Information, Table S2, the R_{ct} value of the TiO_{2-x}NCs interlayer decreases about 6.1 times (from 13676 Ω cm^2 to 2235 Ω cm^2) than the given one. It reduces approximately 3.3-fold than that of the Ti substrate (7299 Ω cm^2, Supporting Information, Figure S3E), implying a promoted charge transfer performance after the doping of Ti^{3+}.[39] The good doping state for increased door density of TiO_{2-x}NCs also could be demonstrated from the Mott–Schottky plot for its shallower slope (Supporting Information, Figure S3F).[40] The presence of Ti^{3+} boosted the formation of a shallow donor level, which is prone to enhancing the carrier density and promoting the charge separation process.[26a] The enlarged CV curves of the TiO_{2-x}NCs layer (Figure 2I) further confirm its improved electrochemical activity. Accordingly, the TiO_{2-x}NCs interlayer can be a suitable matrix for depositing the Sb–SnO_2 catalytic layer.

In scanning electron micrographs (Figure 3A, B), uneven and agglomerated particles with deep cracks can be seen on the Sb–SnO_2 surface. The homogeneity and integrity of the electrode are strongly improved for TiO_{2-x}NCs/Sb–SnO_2 (Figure 3D, E). More specifically, the coating is uniform and compact, with smaller particle sizes, due to the improved current distribution of the TiO_{2-x}NCs middle layer, enhancing its specific surface area to provide more active sites. Elemental mappings show a homogenous distribution of Sn, O, and Sb on the TiO_{2-x}NCs/Sb–SnO_2 surface (Supporting Information, Figure S4B–D), demonstrating the successful formation and synthesis of Sb–SnO_2.

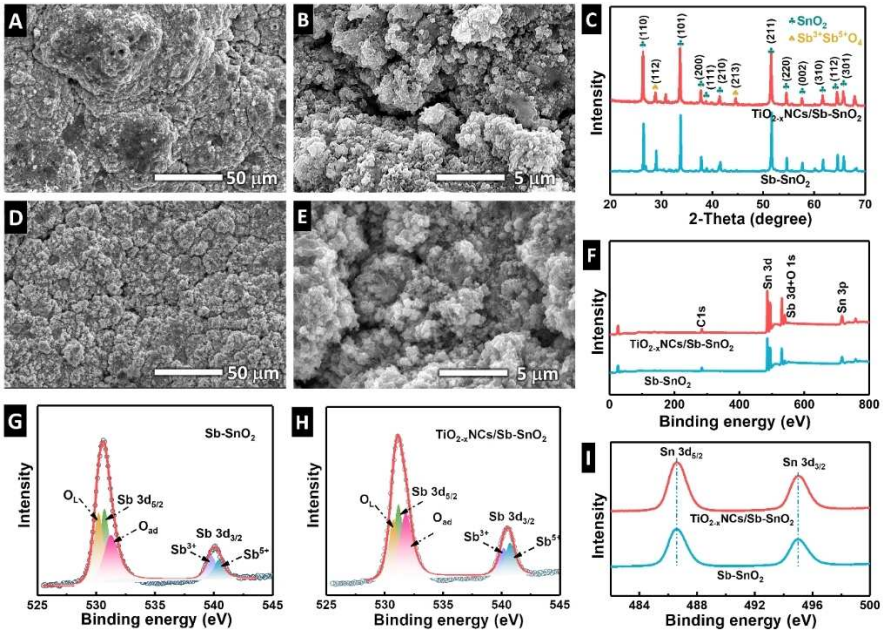

Figure 3. Scanning electron micrographs of Sb–SnO_2 (A and B) and TiO_{2-x}NCs/Sb–SnO_2 (D and E) electrodes. X-ray diffractograms (C), full XPS spectra (F), and the Sn 3d spectra (I) of the prepared electrodes. (G) and (H) are the O 1s spectra of the Sb–SnO_2 and TiO_{2-x}NCs/Sb–SnO_2 electrodes, respectively.

X-ray diffractograms (Figure 3C) confirm the successful preparation of tetragonal rutile SnO_2 (JCPDS No. 41-1445) of the Sb–SnO_2 and TiO_{2-x}NCs/Sb–SnO_2 electrodes. Well-visible diffraction peaks of orthorhombic $Sb^{3+}Sb^{5+}O_4$ (JCPDS No. 11-0694) are at 28.9° 2θ and 44.6° 2θ, revealing the appearance of Sb^{3+} and Sb^{5+}.[41] The Ti-related peaks are not recorded on both anodes, suggesting the good coverage of the Sb–SnO_2 coating.

In Figure 3F, we see the absence of elemental Ti in both full X-ray photoelectron emission spectra of the Sb–SnO_2 and TiO_{2-x}NCs/Sb–SnO_2 anodes, which is in good agreement with the XRD results. Figure 3I displays the detailed spectra of Sn 3d. Two peaks, Sn $3d_{5/2}$ (486.58 eV) and Sn $3d_{3/2}$ (495.02 eV), with a difference of 8.44 eV, can be observed, demonstrating the valence state of Sn is +4.[42] As depicted in Figure 3G and H, the O 1s and Sb 3d signals overlap and are subjected to peak deconvolution to clarify further the composition and chemical valence of the Sb and O elements (Supporting Information, Table S3). The O 1s spectra of the two anodes are composed of two parts, O_L and O_{ad}. The former corresponds to the bonded oxygen with metal atoms, and the latter is related to absorbed hydroxyl oxygen species, which are prone to exchange oxygen with adsorbed molecules. The participation of O_{ad} in the redox reaction process facilitates the generation of •OH to boost the anode oxidation capacity.[43] As seen in Supporting Information, Table S3, the atom ratio of O_{ad}/O_L in the TiO_{2-x}NCs/Sb–SnO_2 anode is about 1.38. This value is higher than the control one, suggesting its excellent •OH generation ability. The Sb 3d spectra contain the Sb $3d_{5/2}$ ground state and the Sb $3d_{3/2}$ excited state. The deconvoluted Sb $3d_{3/2}$ peak indicated the presence of Sb^{5+} and Sb^{3+}, in agreement with the XRD results. The modified electrode also featured a higher proportion of Sb^{5+} with the Sb^{5+}/Sb^{3+} value is 1.17. For comparison: the same value for the Sb–SnO_2 anode is just 0.80. Sb^{5+} ions are easier to enter into the lattice of the SnO_2 matrix to reduce its band gap for the smaller atomic radius than Sb^{3+}. The areas with more Sb^{5+} have high activity for the promoted conductivity and increased amount of physically adsorbed •OH.[44] Accordingly, the modified TiO_{2-x}NCs/Sb–SnO_2 Sb–SnO_2 anode is more suitable for degrading organic pollutants than the Sb–SnO_2 anode.

Electrochemical characterization

Oxygen evolution is a side reaction during the oxidation process, leading to several detrimental effects, including consuming the adsorbed hydroxyl radicals [Eq. (1)] to weaken the oxidation capacity, consuming power to lower the current efficiency, and shortening the electrode service life for the generated oxygen could oxide the Ti substrate.[45]

$$OH_{ad} + H_2O \rightarrow O_2 + 3H^+ + 3e^- \quad (1)$$

Therefore, LSV curves were measured in 0.5 M H_2SO_4 solution to characterize the oxygen evolution performances of the prepared electrodes. In Figure 4A, the TiO_{2-x}NCs/Sb–SnO_2 anode exhibited a strongly enhanced OEP value (from 2.33 V to 2.63 V), which can be attributed to the more significant proportion of O_{ad}.[46] As summarized in Supporting Information, Table S4, the OEP value of the TiO_{2-x}NCs/Sb–SnO_2 electrode is also superior to many other works, like TiO_2-NTs/Sb–SnO_2 (2.05 V vs. SCE),[21] TiO_2-NTs/SnO_2–Sb (1.95 V vs. SCE),[47] suggesting its promising application prospect.

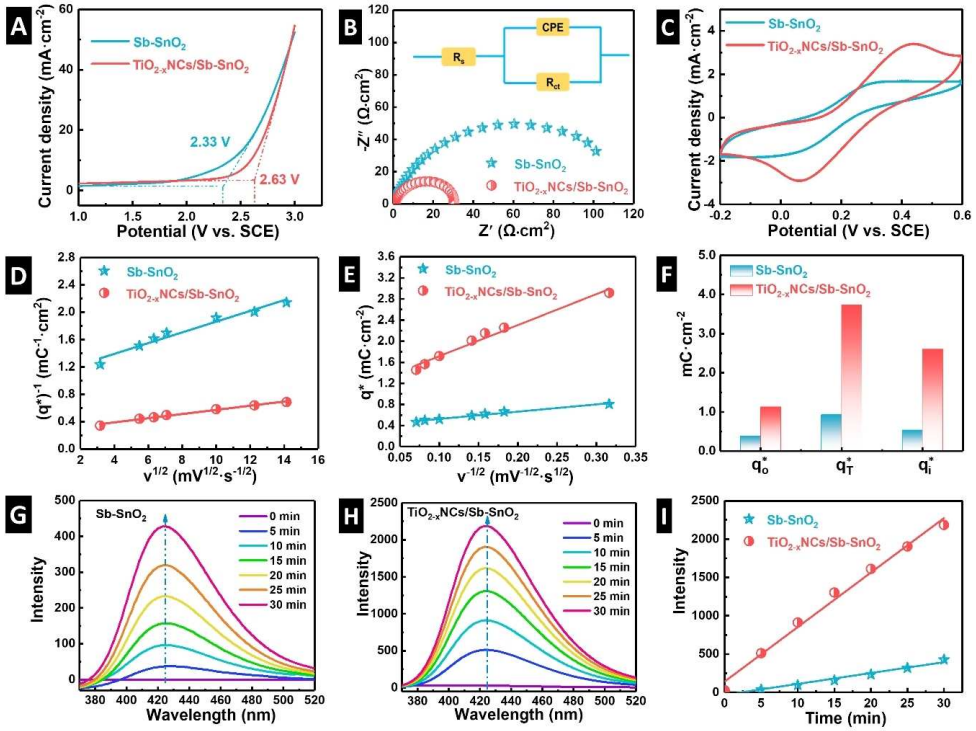

Figure 4. Electrochemical measurements of the Sb–SnO_2 and TiO_{2-x}NCs/Sb–SnO_2 electrodes: Linear sweep voltammetry curves in 0.5 M H_2SO_4 solution at 50 mV s^{-1} (A), Nyquist plots in 0.5 M H_2SO_4 solution at open circuit potential from 10 kHz to 0.01 Hz with 5 mV amplitude (the insert is the corresponding equivalent circuit model) (B), cyclic voltammograms curves from −0.2 V to +0.6 V vs. SCE at 50 mV s^{-1} in 5 mM $K_3[Fe(CN)_6]/K_2[Fe(CN)_4]$ solution with 0.1 M KCl as supporting electrolyte (C). Relationship between $(q^*)^{-1}$ versus $v^{1/2}$ (D) and q^* versus $v^{-1/2}$ (E). The number of different types of voltammetric charges of the prepared anodes (F). Fluorescence spectra of the Sb–SnO_2 (G) and TiO_{2-x}NCs/Sb–SnO_2 (H) electrodes, and the corresponding fluorescence intensity changes versus electrolysis time (I).

We carried out electrochemical impedance spectroscopy to analyze the interfacial impedance of the prepared electrodes in 0.5 M H_2SO_4 solution from 10 kHz to 0.01 Hz. In Figure 4B, we see the presence of semicircles in the Nyquist plots owing to the charge exchange and compensation process at the electrode/electrolyte interface. The much-decreased arc diameter of the modified TiO_{2-x}NCs/Sb–SnO_2 anode suggested its promoted charge transfer performance. The fitting results (Supporting Information, Table S5) show a 4-times decreased R_{ct} value (from 127.5 Ω cm^2 to 31.6 Ω cm^2) compared to the Sb–SnO_2 electrode, resulting from its refined crystallinity and compact morphology.

Cyclic voltammograms were recorded in 0.1 M KCl with 5 mM $K_3[Fe(CN)_6]/K_2[Fe(CN)_4]$ solution as a redox couple to investigate the anode's electrochemical characteristics. As seen in Figure 4C, a couple of well-defined oxidation and reduction peaks with good symmetry are observed on both anodes for prominent reversibility. The enlarged area under the cyclic voltammograms of the TiO_{2-x}NCs/Sb–SnO_2 electrode demonstrated its superior electrochemical activity. We also recorded cyclic voltammograms in 0.25 M Na_2SO_4 solution from 0.6 V to 0.8 V vs. SCE at scan rates from 10 mV s^{-1} to 200 mV s^{-1} to determine the number of active sites. In Supporting Information, Figure S5A and B, we see a nearly rectangular shape from the measured cyclic voltammograms, indicative of capacitive (or pseudocapacitive) processes.[48] The number of active sites is proportional to the amount of voltametric charges (q^*). The total voltametric charge (q_T^*) is composed of two parts, outer voltammetric charge (q_O^*) and inner voltammetric charge (q_i^*). The number of q_T^*, q_O^* and q_i^* can be calculated according to Equations (2)–(4).[49]

$$q^* = q_O^* + k' v^{-1/2} \quad (2)$$

$$(q^*)^{-1} = (q_T^*)^{-1} + k v^{1/2} \quad (3)$$

$$q_T^* = q_O^* + q_i^* \quad (4)$$

In Figure 4D and E, the linear correlations are fitted on both the plots between$(q^*)^{-1}$ and $v^{1/2}$ and the curves between q^* and $v^{-1/2}$. The calculated results are displayed in Figure 4F. The q_T^*, q_O^*, and q_i^* values of the TiO_{2-x}NCs/Sb–SnO_2 electrode are 3.7 mC cm^{-2}, 1.1 mC cm^{-2}, and 2.6 mC cm^{-2}, respectively, which are 4.0, 2.9, and 4.8 times than the Ti/Sb–SnO_2 electrode. These increased amounts of active sites can be ascribed to decreased particle sizes. The value of q_i^*/q_T^* is defined as the anode electrochemical porosity (r).[50] Our TiO_{2-x}NCs/Sb–SnO_2 electrode provides a higher r value (0.70) than the given anode (0.58), facilitating the electrolyte to permeate into the inner active sites to advance the anode degradation capacity.[51]

The •OH radicals generation ability is an important index reflecting the non-active anode oxidation ability. As depicted in Figure 4G and H, with the extension of electrolysis duration, both anodes presented an increased fluorescence intensity of the peak at around 425 nm, suggesting the continuous generation and accumulation of •OH. The evolution of fluorescence intensity with electrolysis time is plotted in Figure 4I. The TiO_{2-x}NCs/Sb–SnO_2 electrode featured a higher fluorescence intensity during the whole electrolysis process. Additionally, the linear fitting results also proved its larger slope (71.1 min^{-1}), which is about 5-times higher than the Sb–SnO_2 electrode (14.2 min^{-1}). The significant promoted •OH radicals generation ability of the TiO_{2-x}NCs/Sb–SnO_2 anode is attributed to its high OEP value, more active sites, and increased amount of O_{ad}.

Electrochemical degradation test

Degradation of cationic dyes

The prepared anodes' degradation performance for cationic dyes, RhB, and MB, was investigated to evaluate their practical application prospect. In Figure 5A and B, the peaks at ~554 nm decrease rapidly with the reaction time since the reduction of RhB. The gradually lighter color of the obtained samples agrees with this observation (Figure 5C). The TiO_{2-x}NCs/Sb–SnO_2 anode featured almost 100% (99.5%) RhB removal efficiency only after 50 min electrolysis and 99.8% after 60 min. The values for the Sb–SnO_2 anode after 50 min and 60 min are much smaller (63.2% and 73.5%, respectively; Figure 5G). The RhB removal process also follows the first-order kinetic model (Supporting Information, Figure S6A); however, the rate constant (k) strongly increases about fivefold from 0.0218 min^{-} to 0.1079 min^{-1} (Supporting Information, Table S6). This value is competitive when compared with other works, such as 3D–Ti/Sb–SnO_2 (0.0493 min^{-1}),[52] Ti/SnO_2–Sb–Ni(2%)/Gd (0.038 min^{-1}),[53] and NiO nanobelts (0.012 min^{-1}).[54]

As demonstrated in the UV/Vis spectrum and sample photos (Figure 5D–F), the TiO_{2-x}NCs/Sb–SnO_2 electrode also achieves a higher MB removal performance for the much-decreased absorbance intensity at ~663 nm and the lighter solution color. The TiO_{2-x}NCs/Sb–SnO_2 electrode achieved 93.6% MB removal efficiency after 120 min electrolysis (Figure 5H) with a higher rate constant (0.0219 min^{-1}) and a shorter half-life time ($t_{MB1/2}$, 31.7 min) than the control Sb–SnO_2 electrode (75.0%, 0.0114 min^{-1}, 60.8 min; Supporting Information, Figure S6B, Table S6). The MB removal rate constant of the modified electrode also comparable with previous reports, for instance, Ti/SnO_2-Sb (0.00952 min^{-1}),[43] BDD (0.01045 min^{-1}),[55] and TiO_2NTA-PbO_2 (0.0189 min^{-1}).[56] These results suggest the

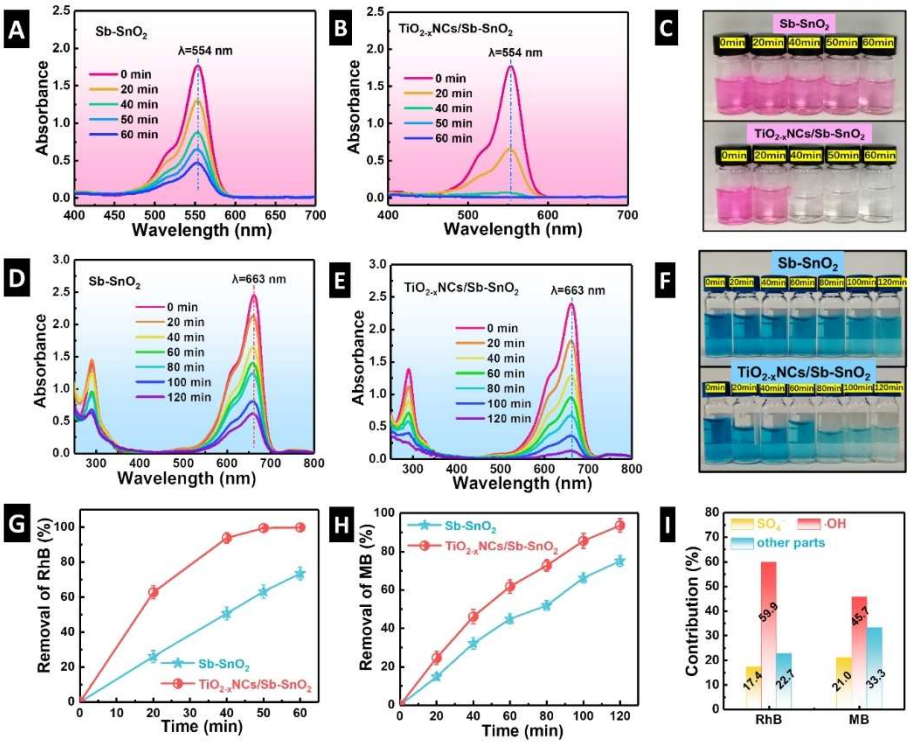

Figure 5. UV/Vis spectra for the degradation of RhB by the Sb–SnO_2 (A) and TiO_{2-x}NCs/Sb–SnO_2 anodes (B); (C) is the corresponding photo of the RhB degradation samples, and (G) the variation of RhB removal efficiency during electrolysis (20 mg L^{-1} RhB, 30 mA cm^{-2}, 40 °C, 10 g L^{-1} Na_2SO_4). UV/Vis spectra for the degradation of MB by the Sb–SnO_2 (D) and TiO_{2-x}NCs/Sb–SnO_2 anodes (E); (F) is the corresponding photo of the MB degradation samples, and (H) the variations of MB removal efficiency during electrolysis (20 mg L^{-1} MB, 30 mA cm^{-2}, 40 °C, 10 g L^{-1} Na_2SO_4). (I) Different radicals' contribution to the removal of RhB and MB.

superior oxidation capacity of the modified TiO_{2-x}NCs/Sb–SnO_2 electrode for the cationic dyes.

An excessive amount of methanol (MeOH; 3 M) and isopropanol (IPA; 3 M) were employed as the scavengers to further clarify the mechanisms for RhB and MB degradation by the TiO_{2-x}NCs/Sb–SnO_2 electrode. MeOH could capture both •OH and $SO_4^{\bullet-}$ for the fast reaction rate constants of 9.7×10^8 L mol^{-1} s^{-1} and 1.0×10^7 L mol^{-1} s^{-1}, respectively. IPA is often utilized to capture only •OH with a higher rate constant (1.9×10^9 L mol^{-1} s^{-1}).[13,57] In Figure 5I, we see that the relative contribution of •OH for RhB and MB degradation are 59.9% and 45.7%, respectively. For $SO_4^{\bullet-}$, the contributions are 17.4% and 21.0%, respectively (see also the Supporting Information). These results confirm the vital role of •OH in the degradation of cationic dyes, and the prominent •OH generation capacity endows the novel TiO_{2-x}NCs/Sb–SnO_2 electrode with satisfactory RhB and MB removal performance. The EPR test results (Supporting Information, Figure S7) also confirmed the existence of •OH and $SO_4^{\bullet-}$ radicals during the RhB degradation process by the TiO_{2-x}NCs/Sb–SnO_2 electrode.[58] Nevertheless, as depicted in Figure 5I, there are still some degradation contributions from other parts, which may be due to the direct oxidation process or the oxidation by other unquenched radicals.[59]

The RhB degradation immediate products of the TiO_{2-x}NCs/Sb–SnO_2 electrode are listed in Supporting Information, Table S7 and the corresponding MS spectrograms are depicted in Supporting Information, Figure S8. The possible degradation mechanisms are displayed in Figure 6, which mainly includes *N*-deethylation, chromophore cleavage, and ring opening. More specifically, pathways I and II have shown a similar degradation process. After a series of *N*-deethylation of RhB, product No. 1 ($m/z=415$), No. 2 ($m/z=387$), No. 3 ($m/z=360$), No. 5 ($m/z=415$) and No. 6 ($m/z=387$) could be produced and further transformed into product No. 4 ($m/z=332$), which is in line with many other works.[60] Due to the attack of •OH, the chromophore groups (xanthene group and phenyl group) were broken and formed many intermediate products (from No. 7 to No. 12).[61] Next, small molecules (from No. 13 to No. 17) were generated by a ring-opening reaction and further mineralized into CO_2 and H_2O.[62]

Degradation of anion dyes

We used AYB and MO as typical anion dye pollutants to evaluate the electrochemical oxidation capacity of the prepared anodes. As a typical anion dye, the azo group (–N=N–) and associated chromophores and auxochromes determine the color generation.[63] As shown in Figure 7A and B, the intensity of the maximum absorption peak located at ~372 nm decreased with the extension of electrolysis time, indicating the broken of the azo bond of AYR, leading to the lightening of the color of the sample (Figure 7C). The other decreased absorption peak at ~270 nm relates to the benzene ring and phenolic hydroxyl group reaction.[64] As such, after 120 min reaction time, a 74.0% and 52.2% removal efficiency of AYR (Figure 7G) can be obtained for the TiO_{2-x}NCs/Sb–SnO_2 and Sb–SnO_2 anodes, respectively, demonstrating the excellent oxidation capacity of the former than the later. The kinetic fitting results also

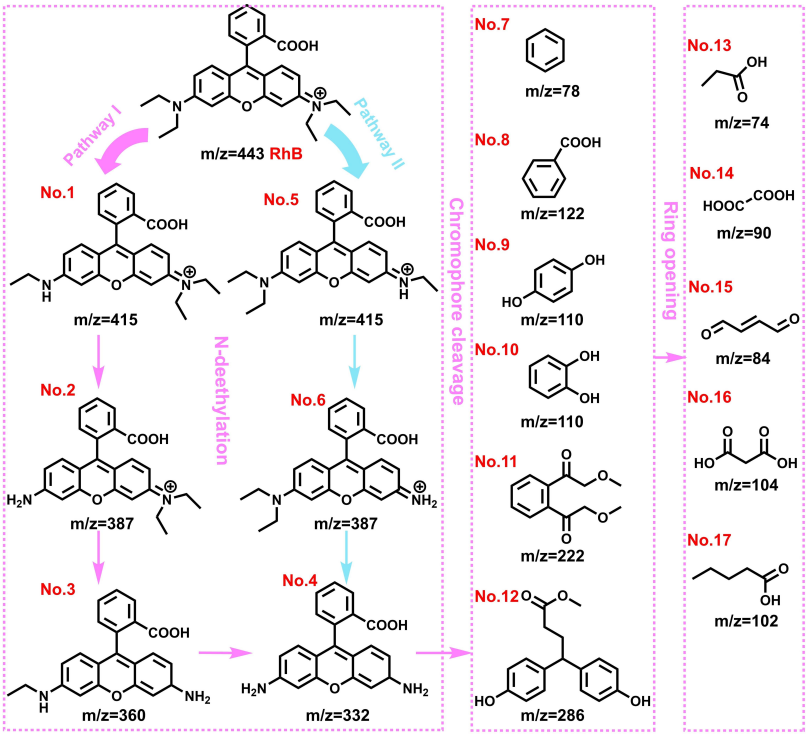

Figure 6. Proposed RhB degradation mechanism by the TiO_{2-x}NCs/Sb–SnO_2 electrode.

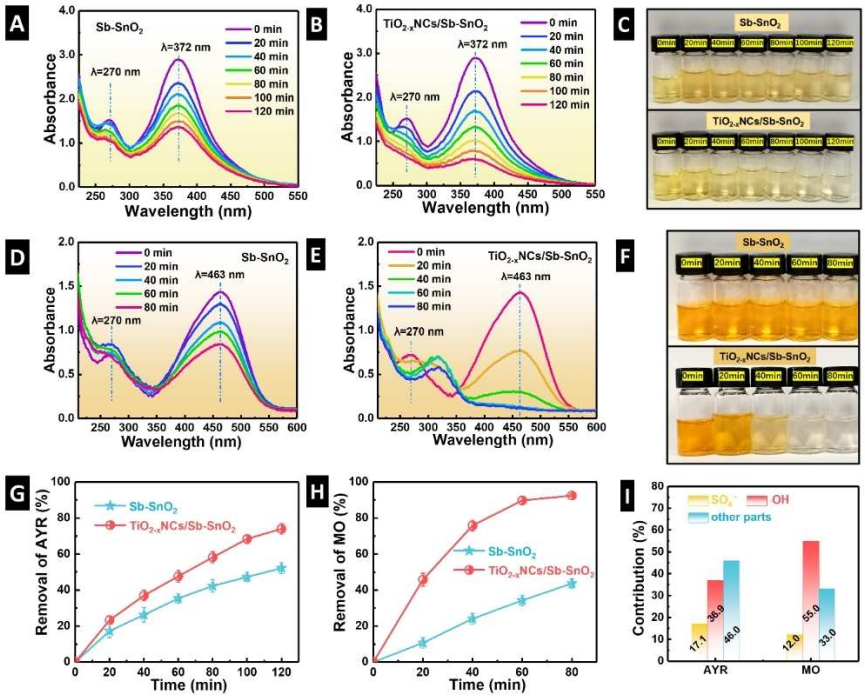

Figure 7. UV/Vis spectra for the degradation of AYR by the Sb–SnO_2 (A) and TiO_{2-x}NCs/Sb–SnO_2 anodes (B); (C) is the corresponding photos of the AYR degradation samples and (G) is the variation of AYR removal efficiency during electrolysis (20 mg L^{-1} AYR, 30 mA cm^{-2}, 40 °C, 10 g L^{-1} Na_2SO_4). UV/Vis spectra for the degradation of MO by the Sb–SnO_2 (D) and TiO_{2-x}NCs/Sb–SnO_2 anodes (E); (F) is the corresponding photo of the MO degradation samples and (H) represents the variations of MO removal efficiency during electrolysis (20 mg L^{-1} MO, 30 mA cm^{-2}, 40 °C, 10 g L^{-1} Na_2SO_4). (I) Different radicals' contribution to the removal of AYR and MO.

confirmed the higher electrocatalytic activity of the TiO_{2-x}NCs/Sb–SnO_2 electrode than the control one (Supporting Information, Figure S9A), with the AYR removal rate constant increased approximately 2-fold from 0.0060 min^{-1} to 0.0111 min^{-1} (Supporting Information, Table S6). We see a higher removal efficiency for the MO degradation by the TiO_{2-x}NCs/Sb–SnO_2 electrode than AYR.

As illustrated in Figure 7D–F, the MO solution also became colorless with the consistent broken of azo bonds at ~463 nm.[65] The peak intensity of ~270 nm of the Sb–SnO_2 electrode did not decrease during the degradation process and even slightly increased after 80 min electrolysis, suggesting the accumulation of benzene rings. However, for the TiO_{2-x}NCs/Sb–SnO_2 electrode, both peaks at ~463 nm and ~273 nm decreased with the reaction time, indicating the simultaneous cleavage of the azo bonds and the benzene rings. These results confirm the good mineralization ability of the TiO_{2-x}NCs/Sb–SnO_2 electrode. Hence, our novel anode achieved 92.5% MO removal efficiency, much higher than the control Sb–SnO_2 electrode (43.7%), as seen in Figure 7H. The corresponding first-order rate constant improved almost fivefold from 0.0073 min^{-1} to 0.0342 min^{-1} (Supporting Information, Figure S9D, and Table S6). The value for the TiO_{2-x}NCs/Sb–SnO_2 electrode also have competitiveness to other reports, 0.0198 min^{-1} for Ti/Sb–SnO_2-4%TiN,[66] 0.0098 min^{-1} for a TiO_2 film,[67] and 0.0135 min^{-1} for PbO_2/SnO_2.[68] The quenching results also demonstrated the important role of •OH in the degradation of AYR and MO, with 36.9% and 55.0%, respectively (Figure 7I). More details are described in Supporting Information.

Two possible degradation pathways for AYR (Figure 8) are also proposed based on the detected intermediates by HPLC-MS (Supporting Information, Figure S10 and Table S8). In Pathway I, due to the existence of the nitro group (strong electron-withdrawing group) and hydroxyl group (strong electron donating group), which could reduce the electron cloud on nitrobenzene, the AYR easily decomposed into product No. 1 (m/z = 123) and product No. 2 (m/z = 165). Then, the •OH radicals attacked the azo double bond of No. 2 to generate product No. 3 (m/z = 153) and further oxidized into No. 4 (m/z = 183).[69] After a series of hydroxylation, decarboxylation and dehydroxylation steps, products No. 5 (m/z = 154), No. 6 (m/z = 110) and No. 7 (m/z = 78) could be formed. Product No. 1 transformed into product No. 8 (m/z = 94) under hydroxylation. Moreover, the attack of •OH to AYR may also generate No. 9 (m/z = 318) and further form No. 10 (m/z = 257).[63] When the azo double bond of No. 10 was broken under the attack of •OH, it may transform into No. 4 and further be oxidized. When the N–C bond of No. 10 was broken, products No. 11 (m/z = 122) and No. 12 (m/z = 137) could be generated owing to the electron-withdrawing effect of –COOH, and then transformed into No. 6 and No. 8, respectively.[70] Simultaneously, the carboxyl group of No.10 may also be firstly removed to generate product No. 13 (m/z = 214), which could further transform into products No. 14 (m/z = 182) and No. 1 (m/z = 123).

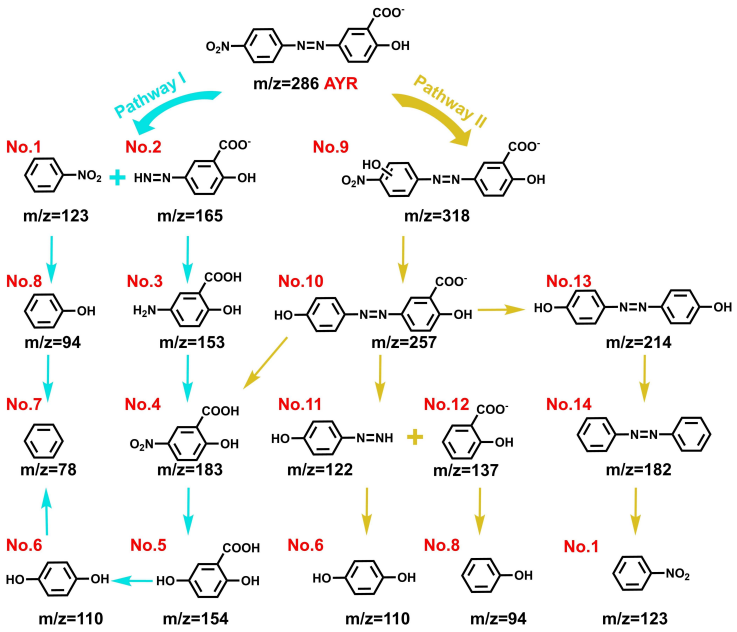

Figure 8. Proposed AYR degradation mechanism by the TiO_{2-x}NCs/Sb–SnO_2 electrode.

Products No. 1, No. 6, and No. 8 could all be degraded into No. 7 and mineralized into CO_2 and H_2O.

Mineralization efficiency and overall energy consumption

The TOC removal efficiency of the degradation samples was analyzed to characterize the anode's deep oxidation ability. As shown in Figure 9A, after electrolysis, the TiO_{2-x}NCs/Sb–SnO_2 anode achieved a higher TOC removal efficiency for RhB (78.2%), MB (67.6%), AYR (47.8%) and MO (63.4%) than the control Sb–SnO_2 electrode where the values are 49.4%, 45.6%, 32.2% and 25.9%, respectively. From Figure 9B, we see that the E_{EO} value for the removal of RhB, MB, AYR, and MO of the TiO_{2-x}NCs/Sb–SnO_2 anode are 1.9 kWh m^{-3}, 9.3 kWh m^{--}, 19.2 kWh m^{-3}, and 6.1 kWh m^{-3}, respectively. All of these values are lower than the control Sb–SnO_2 electrode, and the values are 9.4 kWh m^{-3}, 18.9 kWh m^{-3}, 36.7 kWh m^{-3}, and 29.5 kWh m^{-3}, respectively. The lower energy consumption of TiO_{2-x}NCs/Sb–SnO_2 relates to its high OEP value for the restriction of oxygen evolution side reaction, strong reactive oxygen species generation capacity, and improved charge transfer performance, indicating its promising practical application prospect.

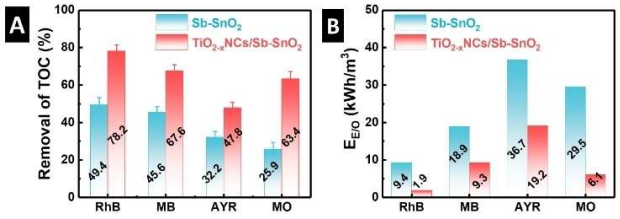

Figure 9. TOC removal efficiency (A) and energy consumption (B) for the degradation of RhB, MB, AYR, and MO.

Anode reusability and stability

Consecutive MO degradation experiments were conducted to evaluate the reusability of the prepared TiO_{2-x}NCs/Sb–SnO_2 anode. In Figure 10A, the anode retained 89.4% MO removal

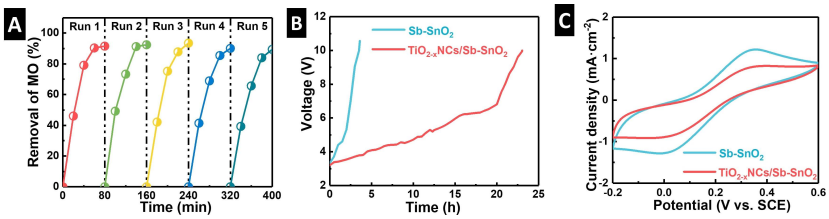

Figure 10. Five times reusability of the prepared TiO_{2-x}NC/Sb–SnO_2 electrode for the degradation of MO (A) (20 mg L^{-1} MO, 30 mA cm^{-2}, 40 °C, 10 g L^{-1} Na_2SO_4). Accelerated lifetime test in 0.5 M H_2SO_4 solution at 50 mA cm^{-2} (B). Cyclic voltammograms of the deactivated Sb–SnO_2 and TiO_{2-x}NCs/Sb–SnO_2 anodes in 5 mM $K_3[Fe(CN)_6]/K_2[Fe(CN)_4]$ solution with 0.1 M KCl as supporting electrolyte at 50 mV s^{-1} (C).

efficiency. In addition, no noticeable decrease occurred after five consecutive degradation experiments, demonstrating its robust durability.

The anode's stability was investigated by accelerated lifetime experiments conducted in 0.5 M H_2SO_4 solution under 100 mA cm^{-2}. In Figure 10B, the lifetime of the novel TiO_{2-x}NCs/Sb–SnO_2 anode is 23 h, which is about sixfold longer than that of the control electrode (3.6 h). Furthermore, the deactivated Sb–SnO_2 anode has a larger closed area under cyclic voltammograms than the deactivated TiO_{2-x}NCs/Sb–SnO_2 anode (Figure 10C), indicating its higher electrochemical activity.

The scanning electron micrograph, EDX spectrum, and the corresponding elemental mappings of the deactivated Sb–SnO_2 electrode are shown in Supporting Information, Figure S11A–C. The exposition of Ti substrate can be observed, indicating the detachment of the Sb–SnO_2 coating, which may be due to the cracks on the anode surface, leading to the permeation of electrolyte and oxygen into the substrate to form nonconductive TiO_2. The generation of TiO_2 would further accelerate the peeling of the coating for the dramatically increased cell voltage. Thus, the Sb–SnO_2 presented a short service time. Nevertheless, for the TiO_{2-x}NCs/Sb–SnO_2 anode, the Ti substrate is entirely covered by the TiO_{2-x}NCs layer even after deactivated (Supporting Information, Figure S11D, E), demonstrating its strong binding force. Ti, O, Sn, and Sb elements are homogeneously distributed across the anode's surface (Supporting Information, Figure S11G). However, the peak intensities of Sn and Sb found in the deactivated TiO_{2-x}NCs/Sb–SnO_2 anode are much lower than the given Sb–SnO_2 anode (Supporting Information, Figure S11F). The elemental ratio analysis also confirmed the former's lower Sn and Sb content than the latter (Supporting Information, Table S9). This result suggests that less Sb–SnO_2 coating survived on the deactivated TiO_{2-x}NCs/Sb–SnO_2 anode surface, leading to a smaller area of the cyclic voltammograms (smaller charge) compared to the deactivated Sb–SnO_2 anode (Figure 10C).

From the obtained data, we can identify two different mechanisms for the anodes deactivation: For the Sb–SnO_2 electrode, the deactivation was caused by the generation of TiO_2; whereas, for the TiO_{2-x}NCs/Sb–SnO_2 anode, the 3D rutile TiO_{2-x}NCs interlayer provided a barrier for the substrate to prevent its oxidation. Hence, the deactivation process mainly resulted from the self-corrosion of the Sb–SnO_2 surface coating, resulting in a longer lifetime. In addition, the good lattice match between TiO_{2-x}NCs and SnO_2 and the concave-convex porous structure strengthens the bond between the interlayer and surface layer. The lower charge transfer resistance of the novel TiO_{2-x}NCs/Sb–SnO_2 anode is also conducive to lowering its cell voltage during the aging test. These factors all resulted in the good stability of the TiO_{2-x}NCs/Sb–SnO_2 electrode.

Conclusions

In this work, a rutile Ti^{3+} self-doped urchin-like TiO_2 nanoclusters (TiO_{2-x}NCs) is first utilized as an interlayer to fabricate a novel TiO_{2-x}NCs/Sb–SnO_2 electrode. This unique 3D matrix structure benefits form a TiO_{2-x}NCs/Sb–SnO_2 anode with a smaller particle size to provide more active sites and significantly enhanced OEP value (from 2.33 V to 2.63 V). This results in a fivefold increase in •OH generation. Accordingly, the rate constants for removing RhB and MO by the novel electrode improved about fivefold compared to the control Sb–SnO_2 anode. Moreover, the TiO_{2-x}NCs/Sb–SnO_2 anode also achieved 93.6% MB and 75.0% AYR removal efficiency after 120 min electrolysis. The quenching experiments confirmed the critical contribution of •OH to the decoloration of these four dyes. The corresponding degradation mechanism of RhB and AYR are all proposed based on the HPLC-MS results. The presence of the rutile TiO_{2-x}NCs interlayer also prolonged the TiO_{2-x}NCs/Sb–SnO_2 anode lifetime by about 6-times for the barrier effect to Ti substrate and the good lattice match to SnO_2. Consequently, we believe this work provides an important design strategy to obtain efficient and stable electrodes for dye wastewater treatment, competitive or superior to, for example, SnO_2, PbO_2, MnO_2, and RuO_2.

Experimental Section

Materials

Ti meshes (> 99.9%, 150 pores per inch) were obtained from Qixin Company Baoji. All reagents and chemicals were of analytical grade and used without further purification. Deionized water (18.25 MΩ cm) was used for all rinses or syntheses.

Preparation of the TiO_{2-x}NCs/Sb–SnO_2 electrode

Ti meshes were ultrasonically cleaned in absolute ethanol and distilled water for 15 min, successively. Then, the TiO_2NCs interlayer was hydrothermally synthesized onto the Ti mesh substrate.[28b] Typically, 0.6 mL titanium isopropoxide, 4 mL acetylacetone, and 0.075 M Na_2EDTA were mixed under constant stirring to form a homogeneous solution. This step was followed by placing the Ti meshes into the polytetrafluoroethylene-lined stainless-steel autoclave (with a volume of 100 mL) and then transferring the above solution into it to heat at 200 °C for 12 h. Then, the obtained samples were washed with water and ethanol and finally annealed in a muffle furnace at 500 °C for 2 h.

The electrochemical reduction process was conducted in 1.0 M $(NH_4)_2SO_4$ solution at 3 mA cm^{-2} for 15 min with the fabricated Ti/TiO_2NCs electrode, and the Pt plate was used as the cathode and anode, respectively.

The Sb–SnO_2 catalytic layer was prepared by electrodeposition technology with the Ti/TiO_{2-x}NCs electrode as the cathode and the Pt plate as the anode. The electrolyte, with a volume of 100 mL, consisted of 0.35 g tartaric acid ($C_6H_6O_6$), 1.5 g of stannic chloride ($SnCl_4$), 0.10 g of antimony trichloride ($SbCl_3$), 0.45 g of gelatin, and 10 g of sodium pyrophosphate anhydrous ($Na_4P_2O_7$). The electrodeposition procedure was carried out at 44 °C for 60 min with a current density of 20 mA cm^{-2}. Finally, the TiO_{2-x}NCs/Sb–SnO_2 could be obtained after annealing at 500 °C for 2 h in an ambient atmosphere. The Sb–SnO_2 electrode was prepared under the same conditions without introducing the TiO_{2-x}NCs interlayer.

Physical and electrochemical characterization

We used a field emission scanning electron microscope coupled with energy-dispersive X-ray spectroscopy (FESEM-EDX; JEOL, JSM-7800F) to investigate the prepared electrodes' surface structure and element distribution. The samples were prepared by fixing the electrodes to a steel holder with the help of conductive adhesive without any sputter coating. The crystal structure was studied by X-ray diffractometer (XRD, PANalytical, X'Pert Powder) with Cu Kα radiation (0.154 nm). The samples were fixed on the holder by assembly putty. The XRD instrument was calibrated with polysilicon wafers before the test. The chemical composition and valence state of elements were examined by X-ray photoelectron spectroscopy (XPS, Thermo ESCALAB 250) using an Al Kα X-ray source (1486.60 eV, 150 W). The electrode samples were adhered to the holder by ordinary double-sided adhesive. The binding energy of the samples was calibrated by the C 1s peak at 284.6 eV. Electron paramagnetic resonance (EPR) spectra were also detected on a Bruker A300 spectrophotometer to characterize the formation of oxygen vacancy. The corresponding *g* values were extracted from simulations by using EasySpin (v5.2.23).

All electrochemical measurements were performed on a CHI660E electrochemical workstation (Shanghai Chenhua Instrument Co.) in a three-electrode configuration. The obtained electrodes, saturated calomel electrode (SCE), and platinum plate (20 mm × 20 mm × 0.2 mm) served as the working electrode, reference electrode, and counter electrode, respectively. Linear sweep voltammetry (LSV) curves were also recorded in 0.5 M H_2SO_4 to measure the electrode OEP values. The charge transfer performance was obtained from electrochemical impedance spectroscopy (EIS) measurements at open circuit potential (OCP) from 10 kHz to 0.01 Hz with a 5 mV amplitude in 0.5 M H_2SO_4 solution. Two electrolytes were adopted to carry out the cyclic voltammograms (CV) tests. One was tested in 5 mM $K_3[Fe(CN)_6]/K_2[Fe(CN)_4]$ with 0.1 M KCl as the supporting electrolyte from −0.2 V to +0.6 V (vs. SCE) at 50 mV s^{-1} to investigate the reversibility and electrochemical activity of the anodes. The other was conducted in 0.25 M Na_2SO_4 from 0.6 V to 0.8 V (vs. SCE) at different scan rates (10, 30, 40, 50, 100, 150, 200 mV s^{-1}) with the potential ranges from 0.6 V to 0.8 V (vs. SCE) to characterize the number of active sites. Mott–Schottky plot was also obtained in 0.25 M Na_2SO_4 from −1 V to 0 V (vs. SCE). The frequency and amplitude were 1 kHz and 10 mV, respectively.

Terephthalic acid was employed as the scavenger to investigate the anode •OH radicals generation performance by measuring the fluorescence intensity of their product (2-hydroxyterephthalic acid). The fabricated SnO_2 electrodes (with an area of 1 cm^2) and Pt plate were also used as the anode and cathode, respectively. The electrolyte was composed of 5 mM terephthalic acid, 0.50 g L^{-1} NaOH and 0.25 mM Na_2SO_4. The applied current density was 30 mA cm^{-2} and the temperature was kept at 30 °C. Sampling was carried out every 5 min. We diluted the specimens 10 times to test the fluorescence intensity from 370 nm to 520 nm with an excitation wavelength of 315 nm by a fluorescence spectrophotometer (Shimadzu RF-6000).

Electrochemical catalytic experiments

All the degradation experiments were performed in a single-compartment cell under constant stirring. The prepared SnO_2 electrodes, with an immersed area of 6 cm^2, were utilized as the anodes, and copper plates, with a distance of 2 cm, served as the cathode. We applied a current density of 30 mA cm^{-2} via a DC power supply (DC, IT6874 A, ITECH). The electrolyte, with a volume of 200 mL, was composed of 20 mg L^{-1} model pollutants (RhB, MB, AYR, and MO) and 10 g L^{-1} Na_2SO_4 as the supporting electrolyte. The temperature was kept at 40 °C. The variations of organics concentration were measured at 554 nm, 663 nm, 372 nm, and 463 nm for RhB, MB, AYR, and MO, respectively, by the UV/Vis spectrophotometer (UV-3600, Shimadzu). The corresponding energy required was calculated by using the electrical efficiency per order ($E_{E/O}$; see also Supporting Information). Total organic carbon (TOC) value changes were monitored by a TOC analyzer (Liqui TOC II, Elementar). The immediate products during RhB and AYR electrolysis were also detected by high-performance liquid chromatography coupled with mass spectrometry (HPLC-MS) (Acquity, Waters) with Agilent Extend C18 column (100 mm × 2.1 mm, 3.5 μm) to investigate the corresponding degradation mechanisms. The injection volume of the samples was 5 μL with a flow rate of 0.5 mL min^{-1}. The wavelengths of the ultraviolet detector were 210 nm and 254 nm. The generated •OH and $SO_4^{\bullet-}$ were identified by EPR with 100 mM 5,5-dimethyl-1-pyrroline N-oxide (DMPO) as the spin-trapping agents.

Accelerated lifetime test

The stability of the prepared anodes was also evaluated by the accelerated lifetime test, which was performed in 0.5 M H_2SO_4 at room temperature. The applied current density was 100 mA cm^{-2}, and the cell voltage increased dramatically to 10 V, which was regarded as the electrode deactivated signal.

Author Contributions

S. M.: Conceptualization, Methodology, Data curation, Writing – original draft; Z. Y.: Validation, Investigation, Data curation, Methodology; S. Z.: Investigation, Data curation, Methodology; E. P.: Visualization, Validation, Writing – review & editing; L. X.: Investigation, Data curation; H. B.: Validation, Resources, Formal analysis; W. Y.: Resources, Project administration; Z. M.: Validation, Project administration; V. P.: Validation, Visualization, Supervision, Writing – review & editing; X. L.: Resources, Project administration, Funding acquisition, Supervision, Writing – review & editing.

Acknowledgments

Shuaishuai Man acknowledges funding from the Chinese Scholarship Council (CSC) via award number 202106050060. Open Access funding enabled and organized by Projekt DEAL.

Conflict of Interest

The authors declare no conflict of interest.

Data Availability Statement

The data that support the findings of this study are available from the corresponding author upon reasonable request.

Keywords: electrochemical oxidation · hydrothermal synthesis · tin oxide · self-doped TiO_2 · wastewater treatment

[1] J. Zhou, Y. Zhang, M. Balda, V. Presser, F.-D. Kopinke, A. Georgi, *Chem. Eng. J.* **2021**, 133544.
[2] a) L. Sun, Y. Mo, L. Zhang, *Chemosphere* **2022**, *294*, 133801; b) Y. Xia, G. Wang, L. Guo, Q. Dai, X. Ma, *Chemosphere* **2020**, *241*, 125010.
[3] Y. L. Feng, H. Wang, J. H. Xu, X. S. Du, X. Cheng, Z. L. Du, H. B. Wang, *J. Hazard. Mater.* **2021**, *416*, 125777.
[4] a) K. Vinothkumar, M. S. Jyothi, C. Lavanya, M. Sakar, S. Valiyaveettil, R. G. Balakrishna, *Chem. Eng. J.* **2022**, *428*, 132561; b) J. Hong, K.-H. Cho, V. Presser, X. Su, *Curr. Opin. Green Sustain. Chem.* **2022**, *36*, 100644.
[5] Z. Li, Y. W. Xie, Y. Zeng, Z. H. Zhang, Y. Y. Song, Z. C. Hong, L. Q. Ma, M. He, H. Ma, F. Y. Cui, *Sci. Total Environ.* **2022**, *806*, 150538.
[6] E. Rosales, M. Pazos, M. A. Longo, M. A. Sanromán, *Chem. Eng. J.* **2009**, *155*, 62–67.
[7] a) A. Ansari, D. Nematollahi, *Appl. Catal. B* **2020**, *261*, 118226; b) S. Man, D. Luo, Q. Sun, H. Yang, H. Bao, K. Xu, X. Zeng, M. He, Z. Yin, L. Wang, Z. Mo, W. Yang, X. Li, *J. Hazard. Mater.* **2022**, *430*, 128440.
[8] X. Ma, Y. Yan, Q. Dai, J. Gao, S. Liu, Y. Xia, *Sep. Purif. Technol.* **2021**, *279*, 119775.
[9] R. Mei, Q. Wei, C. Zhu, W. Ye, B. Zhou, L. Ma, Z. Yu, K. Zhou, *Appl. Catal. B* **2019**, *245*, 420–427.
[10] G. Dong, K. Lang, Y. Gao, W. Zhang, D. Guo, J. Li, D. F. Chai, L. Jing, Z. Zhang, Y. Wang, *J. Colloid Interface Sci.* **2022**, *608*, 2921–2931.
[11] a) S. Man, X. Zeng, Z. Yin, H. Yang, H. Bao, K. Xu, L. Wang, X. Ge, Z. Mo, W. Yang, X. Li, *Electrochim. Acta* **2022**, *411*, 140066; b) S. Deng, Y. Dai, Y. Situ, D. Liu, H. Huang, *Electrochim. Acta* **2021**, *298*, 139335.
[12] S. Man, X. Ge, K. Xu, H. Yang, H. Bao, Q. Sun, M. He, Y. Xie, A. Li, Z. Mo, W. Yang, X. Li, *Sep. Purif. Technol.* **2022**, *280*, 119816.
[13] Q. Zhou, D. Liu, G. Yuan, Y. Tang, K. Cui, S. Jang, Y. Xia, W. Xiong, *Sep. Purif. Technol.* **2022**, *281*, 119735.
[14] a) C. Yang, Y. Fan, S. Shang, P. Li, X.-y. Li, *Environ. Int.* **2021**, *157*, 106827; b) Y. Sun, S. Zhang, B. Jin, S. Cheng, *J. Hazard. Mater.* **2021**, *416*, 125907.
[15] a) C. Yang, Y. Fan, P. Li, Q. Gu, X.-y. Li, *Chem. Eng. J.* **2021**, *422*, 130032; b) G. Wang, H. Zhang, W. Wang, X. Zhang, Y. Zuo, Y. Tang, X. Zhao, *Sep. Purif. Technol.* **2021**, *268*, 118591.
[16] G. H. Zhao, X. Cui, M. C. Liu, P. Q. Li, Y. G. Zhang, T. C. Cao, H. X. Li, Y. Z. Lei, L. Liu, D. M. Li, *Environ. Sci. Technol.* **2009**, *43*, 1480–1486.
[17] M. Moura de Salles Pupo, J. M. Albahaca Oliva, K. I. Barrios Eguiluz, G. R. Salazar-Banda, J. Radjenovic, *Chemosphere* **2020**, *253*, 126701.
[18] L. Huang, D. Li, J. Liu, L. Yang, C. Dai, N. Ren, Y. Feng, *J. Hazard. Mater.* **2020**, *393*, 122329.
[19] L. S. Yang, Z. H. Zhang, J. F. Liu, L. L. Huang, L. Jia, Y. J. Feng, *ChemElectroChem* **2018**, *5*, 3451–3459.
[20] Y. Yang, M. R. Hoffmann, *Environ. Sci. Technol.* **2016**, *50*, 11888–11894.
[21] Y. Guo, T. Duan, Y. Chen, Q. Wen, *Ceram. Int.* **2015**, *41*, 8723–8729.
[22] X. Cui, G. Zhao, Y. Lei, H. Li, P. Li, M. Liu, *Mater. Chem. Phys.* **2009**, *113*, 314–321.
[23] W. Zeng, H. Liang, H. Zhang, X. Luo, D. Lin, G. Li, *Sep. Purif. Technol.* **2022**, *289*, 120720.
[24] a) N. Liu, X. Chen, J. Zhang, J. W. Schwank, *Catal. Today* **2014**, *225*, 34–51; b) X. Du, M. A. Oturan, M. Zhou, N. Belkessa, P. Su, J. Cai, C. Trellu, E. Mousset, *Appl. Catal. B* **2021**, *296*, 120332.
[25] Q. Liu, L. Wang, K. Zhao, W. Yan, M. Liu, D. Wei, L. Xi, J. Zhang, *Electrochim. Acta* **2020**, *354*, 136727.
[26] a) Y. Ma, N. Wang, J. Chen, C. Chen, H. San, J. Chen, Z. Cheng, *ACS Appl. Mater. Interfaces* **2018**, *10*, 22174–22181; b) D. Pang, Y. Liu, H. Song, D. Chen, W. Zhu, R. Liu, H. Yang, A. Li, S. Zhang, *Chem. Eng. J.* **2021**, *405*, 126982.
[27] a) S. Erdemoglu, S. K. Aksu, F. Sayilkan, B. Izgi, M. Asilturk, H. Sayilkan, F. Frimmel, S. Gucer, *J. Hazard. Mater.* **2008**, *155*, 469–476; b) B. Souvereyns, K. Elen, C. De Dobbelaere, A. Kelchtermans, N. Peys, J. D'Haen, M. Mertens, S. Mullens, H. Van den Rul, V. Meynen, P. Cool, A. Hardy, M. K. Van Bael, *Chem. Eng. J.* **2013**, *223*, 135–144.
[28] a) S. S. Man, H. B. Bao, H. F. Yang, K. Xu, A. Q. Li, Y. T. Xie, Y. Jian, W. J. Yang, Z. H. Mo, X. M. Li, *J. Alloys Compd.* **2021**, *859*, 157884; b) R. Song, H. Chi, Q. Ma, D. Li, X. Wang, W. Gao, H. Wang, X. Wang, Z. Li, C. Li, *J. Am. Chem. Soc.* **2021**, *143*, 13664–13674.
[29] L. Wang, L. Wang, Y. Shi, B. Zhao, Z. Zhang, G. Ding, H. Zhang, *Chemosphere* **2022**, *306*, 135628.
[30] a) J. Cai, M. Zhou, Y. Pan, X. Du, X. Lu, *Appl. Catal. B* **2019**, *257*, 117902; b) J. Song, M. Zheng, X. Yuan, Q. Li, F. Wang, L. Ma, Y. You, S. Liu, P. Liu, D. Jiang, L. Ma, W. Shen, *J. Mater. Sci.* **2017**, *52*, 6976–6986; c) C. Kim, S. Kim, J. Choi, J. Lee, J. S. Kang, Y.-E. Sung, J. Lee, W. Choi, J. Yoon, *Electrochim. Acta* **2014**, *141*, 113–119.
[31] Y. Liu, D. Pang, L. Wang, H. Song, R. Liu, S. Hu, Y. Shen, A. Li, S. Zhang, *J. Hazard. Mater.* **2021**, *414*, 125600.
[32] S. A. Abdullah, M. Z. Sahdan, N. Nafarizal, H. Saim, Z. Embong, C. H. Cik Rohaida, F. Adriyanto, *Appl. Surf. Sci.* **2018**, *462*, 575–582.
[33] a) C. Wang, T. Zhang, L. Yin, C. Ni, J. Ni, L. A. Hou, *Chemosphere* **2022**, *286*, 131804; b) X. Cheng, Q. Cheng, B. Li, X. Deng, J. Li, P. Wang, B. Zhang, H. Liu, X. Wang, *Electrochim. Acta* **2015**, *186*, 442–448; c) S. A. Abdullah, M. Z. Sahdan, N. Nayan, Z. Embong, C. R. C. Hak, F. Adriyanto, *Mater. Lett.* **2020**, *263*, 127143.
[34] a) D. N. Pei, L. Gong, A. Y. Zhang, X. Zhang, J. J. Chen, Y. Mu, H. Q. Yu, *Nat. Commun.* **2015**, *6*, 8696; b) C. Zhao, Y. Yang, L. Luo, S. Shao, Y. Zhou, Y. Shao, F. Zhan, J. Yang, Y. Zhou, *Sci. Total Environ.* **2020**, *747*, 141533; c) C. Liu, A. Y. Zhang, D. N. Pei, H. Q. Yu, *Environ. Sci. Technol.* **2016**, *50*, 5234–5242.
[35] a) A. Son, J. Lee, M. G. Seid, E. Rahman, J. Choe, K. Cho, J. Lee, S. W. Hong, *Appl. Catal. B* **2022**, *315*, 121543; b) Z. Dong, D. Ding, T. Li, C. Ning, *Appl. Surf. Sci.* **2019**, *480*, 219–228.
[36] H. Guo, W. Hu, Z. Xu, S. Guo, D. Qiao, X. Wang, H. Xu, W. Yan, *Process Saf. Environ.* **2022**, *164*, 189–207.
[37] S. N. R. Inturi, T. Boningari, M. Suidan, P. G. Smirniotis, *J. Phys. Chem. C* **2013**, *118*, 231–242.
[38] X. Deng, H. Zhang, R. Guo, Q. Ma, Y. Cui, X. Cheng, M. Xie, Q. Cheng, *Sep. Purif. Technol.* **2018**, *192*, 329–339.
[39] D. Yu, Y. Zhang, F. Wang, J. Dai, *RSC Adv.* **2021**, *11*, 2307–2314.
[40] a) Y.-U. Shin, J. Lim, S. Hong, *Desalination* **2022**, *538*, 115899; b) C. Mao, F. Zuo, Y. Hou, X. Bu, P. Feng, *Angew. Chem. Int. Ed.* **2014**, *53*, 10485–10489; *Angew. Chem.* **2014**, *126*, 10653–10657.
[41] H. W. Kim, H. G. Na, J. Bae, J. C. Yang, S. S. Kim, H. Cheong, D. Y. Kim, *Electrochem. Solid-State Lett.* **2012**, *15*, K49.
[42] N. Mameda, H. Park, S. S. A. Shah, K. Lee, C.-W. Li, V. Naddeo, K.-H. Choo, *Chem. Eng. J.* **2020**, *393*, 124794.
[43] Y. Sun, S. Cheng, Z. Mao, Z. Lin, X. Ren, Z. Yu, *Chemosphere* **2020**, *239*, 124715.
[44] S. Man, H. Bao, K. Xu, H. Yang, Q. Sun, L. Xu, W. Yang, Z. Mo, X. Li, *Chem. Eng. J.* **2021**, *417*, 129266.
[45] a) X. Li, Y. Wu, W. Zhu, F. Xue, Y. Qian, C. Wang, *Electrochim. Acta* **2016**, *220*, 276–284; b) H. Zhang, J. Qian, J. Zhang, J. Xu, *J. Alloys Compd.* **2021**, *882*, 160700.
[46] a) Y. Duan, Y. Chen, Q. Wen, T. Duan, *J. Electroanal. Chem.* **2016**, *768*, 81–88; b) T. Wu, G. H. Zhao, Y. Z. Lei, P. Q. Li, *J. Phys. Chem. C* **2011**, *115*, 3888–3898.
[47] Y. Chen, L. Hong, H. Xue, W. Han, L. Wang, X. Sun, J. Li, *J. Electroanal. Chem.* **2010**, *648*, 119–127.
[48] S. Fleischmann, Y. Zhang, X. Wang, P. T. Cummings, J. Wu, P. Simon, Y. Gogotsi, V. Presser, V. Augustyn, *Nat. Energy* **2022**, *7*, 222–228.
[49] G. Lai, C. Zhen, C. Bangyao, S. Yuzhu, Y. Qiang, Z. Wei, H. Qi, L. Yuanyuan, Z. Zhaoyi, Z. Lv, Y. Hongjun, Y. Farhana, *J. Hazard. Mater.* **2020**, *399*, 123018.
[50] L. Xu, M. Li, W. Xu, *Electrochim. Acta* **2015**, *166*, 64–72.
[51] X. Zhang, D. Shao, W. Lyu, G. Tan, H. Ren, *Chem. Eng. J.* **2019**, *361*, 862–873.
[52] S. Asim, Y. Zhu, M. Rana, J. Yin, M. W. Shah, Y. Li, C. Wang, *Chemosphere* **2017**, *169*, 651–659.
[53] T. P. Wai, Y. Yin, X. Zhang, Z. Li, F. Alakhras, *J. Chem.* **2021**, *2021*, 1–18.
[54] N. Kitchamsetti, M. S. Ramteke, S. R. Rondiya, S. R. Mulani, M. S. Patil, R. W. Cross, N. Y. Dzade, R. S. Devan, *J. Alloys Compd.* **2021**, *855*.
[55] M. Wu, G. Zhao, M. Li, L. Liu, D. Li, *J. Hazard. Mater.* **2009**, *163*, 26–31.
[56] C. Yang, S. Shang, X.-y. Li, *Sep. Purif. Technol.* **2021**, *258*, 118035.
[57] F. Chen, L. Xia, Y. Zhang, J. Bai, J. Wang, J. Li, M. Rahim, Q. Xu, X. Zhu, B. Zhou, *Appl. Catal. B* **2019**, *259*, 118071.
[58] Z. H. Xie, C. S. He, H. Y. Zhou, L. L. Li, Y. Liu, Y. Du, W. Liu, Y. Mu, B. Lai, *Environ. Sci. Technol.* **2022**, *56*, 8784–8795.
[59] X. Qian, K. Peng, L. Xu, S. Tang, W. Wang, M. Zhang, J. Niu, *Chem. Eng. J.* **2022**, *429*, 132309.
[60] a) X. Shi, P. Hong, H. Huang, D. Yang, K. Zhang, J. He, Y. Li, Z. Wu, C. Xie, J. Liu, L. Kong, *J. Colloid Interface Sci.* **2022**, *610*, 751–765; b) L. Zhang, Y. Meng, H. Shen, J. Li, C. Yang, B. Xie, S. Xia, *Appl. Surf. Sci.* **2021**, *567*, 150760; c) Y. Liu, H. Guo, Y. Zhang, X. Cheng, P. Zhou, G. Zhang, J. Wang, P. Tang, T. Ke, W. Li, *Sep. Purif. Technol.* **2018**, *192*, 88–98.
[61] Z. He, C. Sun, S. Yang, Y. Ding, H. He, Z. Wang, *J. Hazard. Mater.* **2009**, *162*, 1477–1486.

[62] a) Y. Pang, L. Kong, D. Chen, G. Yuvaraja, S. Mehmood, *J. Hazard. Mater.* **2020**, *384*, 121447; b) A. A. Isari, A. Payan, M. Fattahi, S. Jorfi, B. Kakavandi, *Appl. Surf. Sci.* **2018**, *462*, 549–564.
[63] C. H. Nguyen, C.-C. Fu, R.-S. Juang, *J. Cleaner Prod.* **2018**, *202*, 413–427.
[64] Y. Zhang, P. He, L. P. Jia, C. X. Li, H. H. Liu, S. Wang, S. P. Zhou, F. Q. Dong, *J. Colloid Interface Sci.* **2019**, *533*, 750–761.
[65] T. Tasaki, T. Wada, K. Fujimoto, S. Kai, K. Ohe, T. Oshima, Y. Baba, M. Kukizaki, *J. Hazard. Mater.* **2009**, *162*, 1103–1110.
[66] Y. Duan, Q. Wen, Y. Chen, T. G. Duan, Y. D. Zhou, *Appl. Surf. Sci.* **2014**, *320*, 746–755.
[67] Y. Zhang, J. Wan, Y. Ke, *J. Hazard. Mater.* **2010**, *177*, 750–754.
[68] Y. Liu, C. Gao, L. Liu, T. Yu, Y. Li, *Sep. Purif. Technol.* **2022**, *284*, 120232.
[69] a) B. Liang, Q. Yao, H. Cheng, S. Gao, F. Kong, D. Cui, Y. Guo, N. Ren, D. J. Lee, A. Wang, *Environ. Sci. Pollut. Res. Int.* **2012**, *19*, 1385–1391; b) L. Yang, W. Chen, C. Sheng, H. Wu, N. Mao, H. Zhang, *Appl. Surf. Sci.* **2021**, *549*, 149300.
[70] B. Zhao, H. B. Yu, Y. Lu, J. Qu, S. Y. Zhu, M. X. Huo, *J. Taiwan Inst. Chem. Eng.* **2019**, *100*, 144–150.

Manuscript received: October 12, 2022
Revised manuscript received: December 8, 2022
Accepted manuscript online: December 16, 2022
Version of record online: January 13, 2023